symmetry

IMPACT FACTOR 2.7

CITESCORE 4.9

Article

Cosmic Ray Anisotropy and Spectra as Probes for Nearby Sources

Aifeng Li, Wei Liu and Yiqing Guo

MDPI

https://doi.org/10.3390/sym16020236

symmetry

MDPI

Article

Cosmic Ray Anisotropy and Spectra as Probes for Nearby Sources

Aifeng Li [1], Wei Liu [2,3,4,*] and Yiqing Guo [2,3,4,*]

[1] College of Information Science and Engineering, Shandong Agricultural University, Taian 271018, China; liaf@sdau.edu.cn
[2] Key Laboratory of Particle Astrophysics, Institute of High Energy Physics, Chinese Academy of Sciences, Beijing 100049, China
[3] University of Chinese Academy of Sciences, Beijing 100049, China
[4] TIANFU Cosmic Ray Research Center, Chengdu 610000, China
* Correspondence: liuwei@ihep.ac.cn (W.L.); guoyq@ihep.ac.cn (Y.G.)

Abstract: Cosmic ray (CR) spectra and anisotropy are closely related to the distribution of CR sources, making them valuable probes for studying nearby sources. There are 12 nearby sources located within 1 kpc of the solar system, and which ones are the optimal candidates? In this work, we have selected the Geminga, Monogem, Vela, Loop I, and Cygnus SNR sources as the focus of our research, aiming to identify the optimal candidate by investigating their contribution to the energy spectra and anisotropy using the Spatially Dependent Propagation (SDP) model. Additionally, the anisotropic diffusion effect of the local regular magnetic field (LRMF) on CR particles is also considered in the SDP model. Our previous work only provided 1D anisotropy along the right ascension; this current work will further present 2D anisotropy maps along the right ascension and declination. When the injection power of different nearby sources is roughly equal, the results show that the Geminga, Momogem, and Loop I SNR sources contribute significantly to the nuclear energy spectra. Under the isotropic diffusion without considering the LRMF, the 2D anisotropy maps indicate that the phase points to the nearby source below 100 TeV. We further adjust the injection power of the Monogem SNR source in accordance with the spin-down energy of the Geminga and Monogem pulsars, and find that the contribution of the corrected Monogem SNR can be disregarded. Because the Loop I SNR source is located in the direction of the Galactic Center (GC), it cannot contribute to the excess of CRs in the anti-GC direction. Under anisotorpic diffusion with the consideration of the LRMF, the 2D anisotropy maps show that only the Geminga SNR can match the anisotropy measurement, while the other sources cannot. Finally, we conclude that the Geminga SNR source is the optimal nearby source.

Keywords: galactic cosmic rays; nearby source; cosmic ray anisotropy; cosmic ray spectra

Citation: Li, A.; Liu, W.; Guo, Y. Cosmic Ray Anisotropy and Spectra as Probes for Nearby Sources. *Symmetry* **2024**, *16*, 236. https://doi.org/10.3390/sym16020236

Academic Editor: M. D. Rodriguez Frias

Received: 10 January 2024
Revised: 6 February 2024
Accepted: 8 February 2024
Published: 15 February 2024

1. Introduction

CRs less than PeV are generally believed to be produced in the Galaxy, and supernova remnants (SNRs) are considered to be the most important galactic sources [1]. CRs can be accelerated to form power-law spectra through the diffusive shock acceleration mechanism at SNRs [2]. The CR spectrum is an important tool for investigating the origin, acceleration, and propagation of CRs. In recent years, with the improvement of the new generation of CR detection technology, numerous space experiments have uncovered subtle anomalies of CR spectra at about 200 GeV, deviating from the expected power-law spectrum. Experiments such as ATIC-2 [3], CREAM [4,5], PAMELA [6], AMS-02 [7,8], and the calorimeter experiment CALET [9] have revealed nuclear spectra become hard at $\mathcal{R}\sim$200 GV, while DAMPE [10,11], CREAM [12], and NUCLEON [13] have found that proton and helium spectra become soft at $\mathcal{R}\sim$14 TV. So far, several theoretical models have been proposed to explain these spectral anomalies, including the contribution of nearby sources near the solar system to the "bulge" of the CR spectra [14,15], interaction between CRs and accelerating

shock waves [16,17], the effect of CR propagation process [15,18], and the superimposition of multiple acceleration sources [19,20].

In addition to the CR energy spectrum, anisotropy is also an important probe for studying CRs. Most of the charged particles in CRs, during their propagation, are subject to deflection and modulation by the galactic magnetic field, and interact with the interstellar medium. As a result, when they reach Earth, they exhibit overall isotropy. However, some ground-based air shower arrays and underground muon detectors, such as Tibet [21–23], Super-Kamiokande [24], Milagro [25,26], IceCube/Ice-Top [27–31], ARGO-YBJ [32,33], EASTOP [34], KASCADE [35,36], and HWAC [37,38] have observed small anisotropy with relative amplitudes of the order of 10^{-4}∼10^{-3} at energies from 100 GeV to hundreds of PeV. The experimental results indicate a complex energy dependence in the amplitude and phase of anisotropy. As the energy increases, the amplitude increases below 10 TeV, decreases from 10 TeV to 100 TeV, and increases again above 100 TeV. Meanwhile, at less than 100 TeV, the phase points towards ∼3 h, which is consistent with the direction of LRMF observed by the IBEX experiment [39], while it points towards the GC above the 100 TeV. In the Multi-TeV energy region, the 2D anisotropy maps obviously present two large-scale structures, which are "beyond" from the heliospheric magnetic tail direction named "Tail-in" and "missing" from the galactic North Pole direction termed "Loss-cone" [21,23]. Generally, the origin of anisotropy may stem from the following factors: nearby sources near the solar system [15,40], the deflection of a local regular magnetic field [40–42], CR propagation [15], and the Compton–Getting effect caused by the relative motion between the Earth's rotation and CRs [22,43].

CR spectra and anisotropy from GeV to ∼100 TeV have some common anomalous characteristics, suggesting that they may have a common origin. In recent years, a large number of studies have revealed that nearby sources are closely related to these anomalies. The work in ref. [40] shows that the Geminga source and the anisotropic diffusion of CRs induced by the LRMF can explain both nuclear spectra and anisotropy. The study in ref. [44] indicates that the Geminga SNR is the sole optimal candidate, while the status of the Monogem SNR is controversial due to the disparity in anisotropy between the model calculation and the observations. Moreover, the Vela SNR contributes to a new spectral structure beyond TeV energy. The work in ref. [45] demonstrates that only the Geminga SNR could be the proper candidate for the local CR source by a fitting calculation. The work in ref. [46] has found that Monogem can reasonably account for primary electron excess and proton spectrum. The work in ref. [42] presents that an excellent candidate for the local CR source responsible for the dipole anisotropy at 1∼100 TeV is the Vela SNR. We found that the age, location, and injection power of nearby sources are crucial in contributing to the energy spectrum and anisotropy.

In the conventional diffusion propagation model of CRs, the non-uniform distribution of CR background sources predicts large-scale anisotropy. Under isotropic diffusion, the anisotropy amplitude increases with energy, and the phase always points towards the GC, which is clearly inconsistent with experimental observations. For example, at ∼100 TeV, the expected amplitude is two orders of magnitude higher than what is observed in experiments. If a nearby source, such as the Geminga SNR, is introduced in the anti-GC direction in the propagation model, it can counterbalance the CR flux from the GC direction, thus helping to alleviate the discrepancies between the theoretical predictions and experimental observations. Another solution for this issue is the SDP model, which diminishes the anisotropy amplitude because of the lower diffusion coefficient in the inner halo compared to the outer halo, but it does not resolve the low-energy phase issue [15]. By observing neutral particles passing through the heliosphere boundary, the IBEX experiment revealed that the LRMF follows $(l, b = 210.5°, -57.1°)$, in the range of 20 pc around the solar system [39,47]. The direction of the LRMF is coincident with the phase of anisotropy below 100 TeV. Several studies [42,47,48] have demonstrated that this coincidence is due to anisotropic diffusion, which guides CRs to propagate along the LRMF. Therefore, in this

work, we establish a unified model that incorporates the effects of nearby sources and the anisotropic diffusion induced by the LRMF based on the SDP model.

There are 12 nearby sources located within 1 kpc of the solar system, and for this study, we have selected Geminga, Monogem, Vela, Loop I, and Cygnus, as listed in Table 1 as the focus of our investigation. The objective of this study is to identify the optimal candidate source by analyzing their contribution to CRs' spectra and anisotropy using the unified propagation model. Our previous work [40] focused solely on studying the 1D anisotropy phase along the right ascension. This current study will further investigate 2D anisotropy maps along the right ascension and declination. This paper is organized as follows: Section 2 presents the model description and methods; in Section 3, the results of CR spectra and anisotropy are presented and discussed; Section 4 gives the summary.

Table 1. The location and age of the five known SNRs. References: 1 [49], 2 [50], 3 [51], 4 [52], 5 [53].

SNR	l	b	d	T_{age} $[pc]$	Ref $[Kyr]$
Geminga	194.3°	−13.1°	330	345	1
Monogem	203.0°	12.0°	288	86	2
Vela	263.9°	−3.3°	295	11	3
Loop I	329.0°	17.5°	170	200	4
Cygnus Loop	74.0°	−8.5°	540	10	5

2. Model and Methods

2.1. Spatially Dependent Diffusion

After being accelerated in the "source" region, the primary CRs enter interstellar space and undergo frequent scattering by the interstellar turbulent magnetic field, resulting in random walks within the galaxy. This random process is known as CR diffusion propagation. The region in which CRs diffuse within the Galaxy is known as the magnetic halo, often approximated as a cylinder with a radial boundary equal to the galactic radius, i.e., $R = 20$ kpc, and a half thickness z_h of a few kpc. The value of z_h is typically determined by fitting the B/C ratio along with the diffusion coefficient [54]. Both CR sources and the interstellar medium are typically assumed to be concentrated near the galactic disk, with an average thickness z_s of approximately 0.2 kpc. CRs in the magnetic halo go through diffusion, convection, reacceleration, energy loss, nuclear and nucleonic fragmentation, as well as the decay of unstable secondary particles. This comprehensive process can be described by the propagation equation [54]. In the conventional propagation model, the diffusion coefficient is a scalar that depends solely on rigidity. This model has successfully explained the cosmic ray power-law spectrum, the B/C ratio, and the distribution of diffuse gamma rays and so on. However, growing experimental observations have challenged the conventional model.

In the past few years, the SDP model with two halos has attracted much attention and been applied to more and more CR research fields. It was originally introduced to account for the spectral hardenings of proton and helium at ∼200 GeV [18]. Afterwards, it was further used to explain the excess of secondary and heavier components [55–58], diffuse gamma ray distribution [59], and large-scale anisotropy [15,45]. Recent measurements of the TeV halo around the pulsar have found that CRs diffuse significantly slower than the inferred boron–carbon ratio, which strongly supports the SDP model [60,61].

In the SDP model, the galactic diffusion halo is divided into two regions, i.e., inner halo (IH) and outer halo (OH). The galactic disk and its surrounding region is called the IH, while the diffusion region outside the IH is called the OH. In the IH region, where there are more sources, the activity of supernova explosions will lead to more intense turbulence. Therefore, the diffusion of CRs will be slow, and the diffusion coefficient will be

less dependent on the rigidity. Whereas in OH region, the diffusion of CRs is less affected by stellar activity, and the diffusion coefficient is consistent with the traditional propagation model and only depends on rigidity.

In this work, we adopt the SDP model and the diffusion coefficient is parameterized as [58,59]

$$D_{xx}(r,z,\mathcal{R}) = D_0 F(r,z)(\frac{\mathcal{R}}{\mathcal{R}_0})^{\delta_0 F(r,z)} \tag{1}$$

where r and z are cylindrical coordinates, $\mathcal{R}$ is particle's rigidity, and D_0 is a constant. The total half-thickness of the propagation halo is z_0, and the half-thickness of the IH is ξz_0. The parameterization of $F(r,z)$ can be parameterized as

$$F(r,z) = \begin{cases} g(r,z) + [1-g(r,z)](\frac{z}{\xi z_0})^n, & |z| \le \xi z_0 \\ 1, & |z| > \xi z_0 \end{cases} \tag{2}$$

where $g(r,z) = N_m/[1+f(r,z)]$, and $f(r,z)$ is the source density distribution.

In this work, we adopt numerical package DRAGON to solve the transport equation [62].

2.2. Background Sources

SNRs are considered the most likely sites for the acceleration of GCRs, where charged particles are accelerated to a power-law distribution through diffusive shock acceleration. The spatial distribution of the background sources are approximated as axisymmetric, following the distribution of SNRs [63]:

$$f(r,z) \propto (r/r_\odot)^{1.69} \exp[-3.33(r-r_\odot)/r_\odot] \exp(-|z|/z_s), \tag{3}$$

where $r_\odot = 8.5$ kpc represents the distance from the solar system to the GC and $z_s = 0.2$ kpc. Formula (3) indicates that the density distribution of the SNRs decreases exponentially along the vertical height from the galactic plane.

The injection spectrum of background sources is assumed to be a power-law of rigidity with a high-energy exponential cutoff, $q(\mathcal{R}) \propto \mathcal{R}^{-\nu} \exp(-\mathcal{R}/\mathcal{R}_c)$. The cutoff rigidity of each element could be either Z- or A-dependent.

2.3. Nearby Source

We solve the time-varying propagation equation of CRs from nearby sources assuming a spherical geometry with infinite boundary conditions and using Green's function method [64,65].

The CR density of nearby sources as a function of the location, time, and rigity is described by

$$\phi(r,\mathcal{R},t) = \frac{q_{\rm inj}(\mathcal{R})}{(\sqrt{2\pi}\sigma)^3} \exp\left(-\frac{r^2}{2\sigma^2}\right), \tag{4}$$

where $q_{\rm inj}(\mathcal{R})\delta(t)\delta(\mathbf{r})$ is the instantaneous injection spectrum of a point source, $\sigma(\mathcal{R},t) = \sqrt{2D(\mathcal{R})t}$ is the effective diffusion length within time t, and $D(\mathcal{R})$ is the diffusion coefficient, which is adopted as the value nearby the solar system. The injection spectrum is also parameterized as a cutoff power-law form, $q_{\rm inj}(\mathcal{R}) = q_0 \mathcal{R}^{-\alpha} \exp(-\mathcal{R}/\mathcal{R}_c')$. The normalization q_0 is obtained through fitting to the CR energy spectra.

2.4. Anisotropic Diffusion and Large-Scale Anisotropy

The amplitude of the dipole anisotropy is proportional to the spatial gradient of the CR density and the diffusion coefficient. In the conventional propagation model, the anisotropy can be written as [42,48]

$$\delta = \frac{3D}{v}\frac{\nabla\psi}{\psi}\,. \tag{5}$$

The Larmor radius of PeV CRs is much smaller than their scattering length in the LRMF, which indicates that the LRMF can deflect the PeV CR particles. CRs diffuse anisotropically in the local interstellar space under the influence of the LRMF, and the diffusion tensor D_{ij} associated with the magnetic field is written as

$$D_{ij} \equiv D_{\perp}\delta_{ij} + (D_{\parallel} - D_{\perp})b_i b_j\,,\ \ b_i = \frac{B_i}{|\vec{B}|} \tag{6}$$

where $D_{\parallel}$ and $D_{\perp}$ are the diffusion coefficients aligned parallel and perpendicular to the ordered magnetic field, b_i is the i-th component of the unit vector [66], respectively. In this work, the values of $D_{\parallel}$ and $D_{\perp}$ are parameterized as power-law function of rigidity, and are shown as follows [40,67]:

$$D_{\parallel} = D_{0\parallel}\left(\frac{\mathcal{R}}{\mathcal{R}_0}\right)^{\delta_{\parallel}}, \tag{7}$$

$$D_{\perp} = D_{0\perp}\left(\frac{\mathcal{R}}{\mathcal{R}_0}\right)^{\delta_{\perp}} \equiv \varepsilon D_{0\parallel}\left(\frac{\mathcal{R}}{\mathcal{R}_0}\right)^{\delta_{\perp}}, \tag{8}$$

where $\varepsilon = \dfrac{D_{0\perp}}{D_{0\parallel}}$ is the ratio between the perpendicular and parallel diffusion coefficient at the reference rigidity $\mathcal{R}_0$. Some works have studied the value of ε, $\delta_{\parallel}$, and $\delta_{\perp}$ [64,68,69]. When $D_{\perp}/D_{\parallel} \ll 1$, the perpendicular diffusion coefficient is much smaller than the parallel one, and CRs are more likely to diffuse along the magnetic field. When $D_{\perp}/D_{\parallel} \approx 1$, the perpendicular diffusion is close to the parallel one, and CRs diffuse almost isotropically.

Under the anisotropic diffusion model, the form of Formula (5) can be written as

$$\delta = \frac{3}{v\psi}D_{ij}\frac{\partial\psi}{\partial x_j}\,. \tag{9}$$

3. Results and Discussion

3.1. Proton and Helium Spectra of Five Nearby Sources

The spatial scale of the LRMF is 20 pc, which is much smaller than the average propagation length of CRs, so the LRMF has almost no effect on the energy spectrum [47]. Therefore, the SDP model under isotropic diffusion can be used to calculate the energy spectra of background sources and nearby sources.

We obtained the propagation parameters by fitting the B/C ratio. Figure 1 presents the comparison of the B/C ratio between the model prediction and the observation data of AMS-02. The corresponding propagation parameters are, respectively, $D_0 = 4.87 \times 10^{28}$ cm^2, $\delta_0 = 0.58$, $N_{\rm m} = 0.62$, $\xi = 0.1$, $n = 4$. The Alfvénic velocity is $v_A = 6$ km $\cdot$ s^{-1}, and the half-thickness of the propagation halo is $z_h = 5$ kpc.

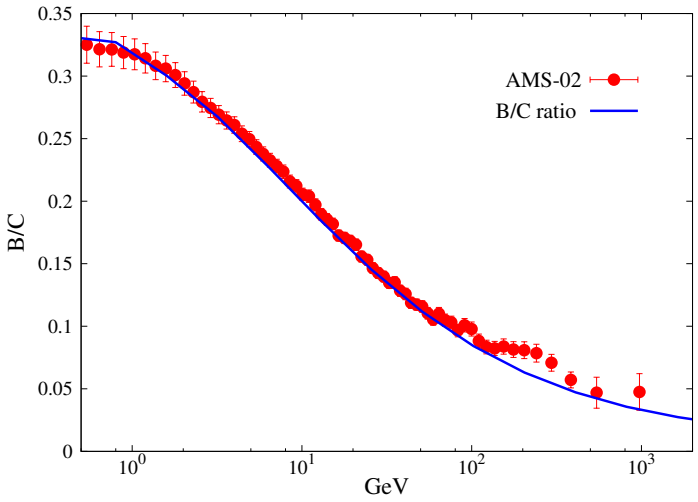

Figure 1. Fitting to B/C ratio with the model prediction. The B/C data points are taken from AMS-02 experiment [70].

First, we calculate the proton and helium spectra with the contribution from five different nearby sources, as listed in Table 1. The Z-dependent cutoff is applied to the injection spectra of the background and nearby sources with a high-energy exponential cutoff. The normalization, power index, and cutoff rigidity are obtained by fitting the energy spectra assuming that the injection power of each source is roughly equal. The corresponding injection parameters of different nuclei in the background and nearby sources are shown in Table 2. Only the injection spectra for the Geminga and Monogem sources are listed here. Figure 2 presents the spectral results of proton (left) and helium (right), where the solid gray line is the contribution of the background sources, the dashed lines in different colors represent the contributions from different single nearby sources, and the solid lines in corresponding colors display the sum of the single nearby sources and background sources. It can be seen that the contribution of the Geminga, Monogem, and Loop I SNR can account for the spectral hardening at ∼200 GeV and softening features at ∼10 TeV, but Vela and Cygnus cannot. This is because the Vela and Cygnus sources are younger than the others, and the low-energy CRs produced by them reach the solar system with difficulty.

Table 2. Injection parameters of the background and nearby sources.

	Background			**Geminga Source**			**Monogem Source**		
Element	**Normalization** †	ν	$\mathcal{R}_c$	q_0	α	$\mathcal{R}'_c$	q_0	α	$\mathcal{R}'_c$
	$(\mathbf{m^2 srs GeV})^{-1}$		**PV**	$\mathbf{GeV}^{-1}$		**TV**	$\mathbf{GeV}^{-1}$		**TV**
p	1.91×10^{-2}	2.34	7	8.28×10^{52}	2.16	25	2.94×10^{52}	2.20	22
He	1.43×10^{-3}	2.27	7	2.35×10^{52}	2.08	25	1.80×10^{52}	2.18	22
C	6.15×10^{-5}	2.31	7	7.2×10^{50}	2.13	25	6.00×10^{50}	2.13	22
N	7.67×10^{-6}	2.34	7	1.13×10^{50}	2.13	25	7.50×10^{49}	2.13	22
O	8.20×10^{-5}	2.36	7	1.11×10^{51}	2.13	25	1.11×10^{51}	2.13	22
Ne	8.05×10^{-6}	2.28	7	1.13×10^{51}	2.13	25	1.13×10^{50}	2.13	22
Mg	1.62×10^{-5}	2.39	7	1.08×10^{50}	2.13	25	1.08×10^{50}	2.13	22
Si	1.28×10^{-5}	2.37	7	1.05×10^{50}	2.13	25	1.05×10^{50}	2.13	22
Fe	1.23×10^{-5}	2.29	7	2.20×10^{50}	2.13	25	2.20×10^{50}	2.13	22

† The normalization is set at total energy $E = 100$ GeV.

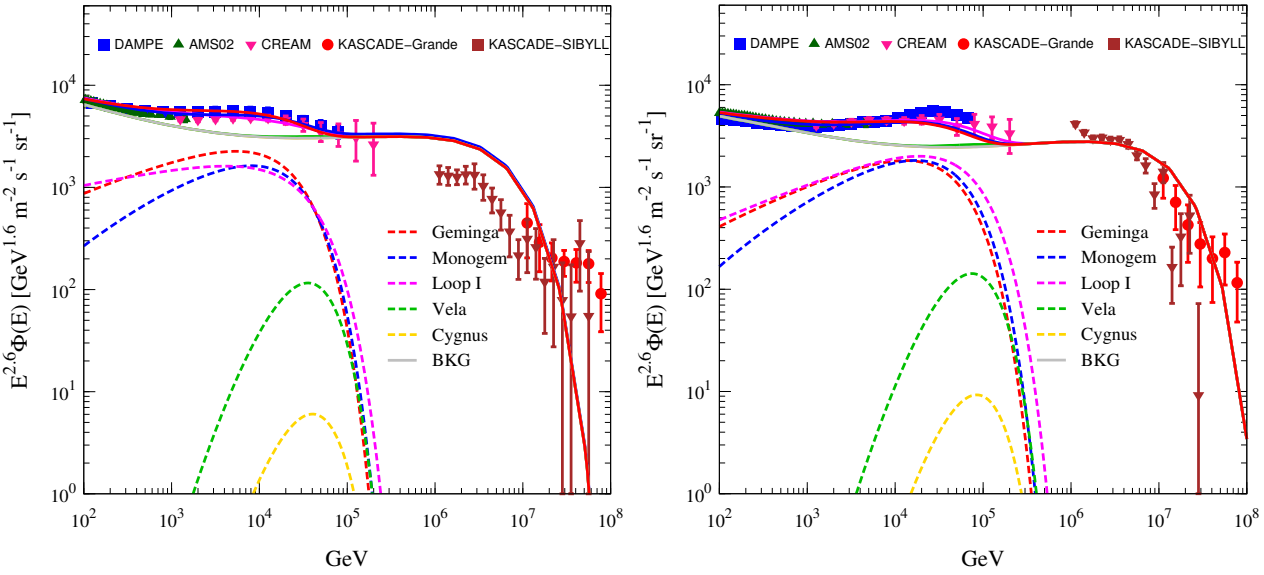

Figure 2. The energy spectra of protons (**left**) and helium nuclei (**right**) with the contribution from five different nearby sources. The data points are taken from DAMPE [10,11], AMS-02 [13,71], CREAM-III [12], NUCLEON [72], KASCADE [73], and KASCADE-Grande [74], respectively. The grey solid lines (BKG) represent the fluxes of background sources, and the dashed lines in different colors are the fluxes from different single nearby SNR sources, respectively, and the solid lines of corresponding color represent the sum contributions of the background and nearby sources.

3.2. Anisotropy of Geminga, Monogem, and Loop I

Given only the energy spectra of the Geminga, Monogem, and Loop I SNR sources are consistent with the experimental data, we will only analyze the anisotropy of these three sources next.

Unlike the energy spectrum, LRMFs clearly deflect CR particles and affect the anisotropy within the concerned energy region, so the LRMF must be considered in the calculation of anisotropy. The parameters of the parallel diffusion coefficient $D_{\parallel}$ are set as those in Section 2.1. After conducting numerous trial studies on the diffusion coefficient, we set $D_{\parallel} > D_{\perp}$, $\varepsilon = 0.01$ and the difference between $\delta_{\perp}$ and $\delta_{\parallel}$ is 0.32, which, due to the CRs from the TeV to PeV energy region are thought to travel faster parallel to the magnetic field than perpendicular to it [40].

Figure 3 illustrates the evolution of the amplitude and phase of anisotropy with energy, taking into account the contribution from the Geminga SNR source. It is evident that the computational results align well with the experimental data. These results further support our previous conclusion regarding the spectra and anisotropy with the contribution from the Geminga SNR [40].

In order to understand the phase along the declination, we further calculate 2D anisotropy maps at 10 TeV and 3 PeV, and the results are shown in Figure 4. We compare the 2D anisotropy maps under isotropic diffusion with those under anisotropic diffusion. The phase points to the Geiminga SNR source under isotropic diffusion, while it points in the direction of the LRMF under anisotropic diffusion at 10 TeV, which is consistent with the experimental observation. This indicates that the LRMF can deflect CR particles below 100 TeV. At 3 PeV, the phase is always directed towards the GC under any diffusion, which is attributed to the fact that the background sources are dominant, and the LRMF cannot deflect the CR particles in this energy region.

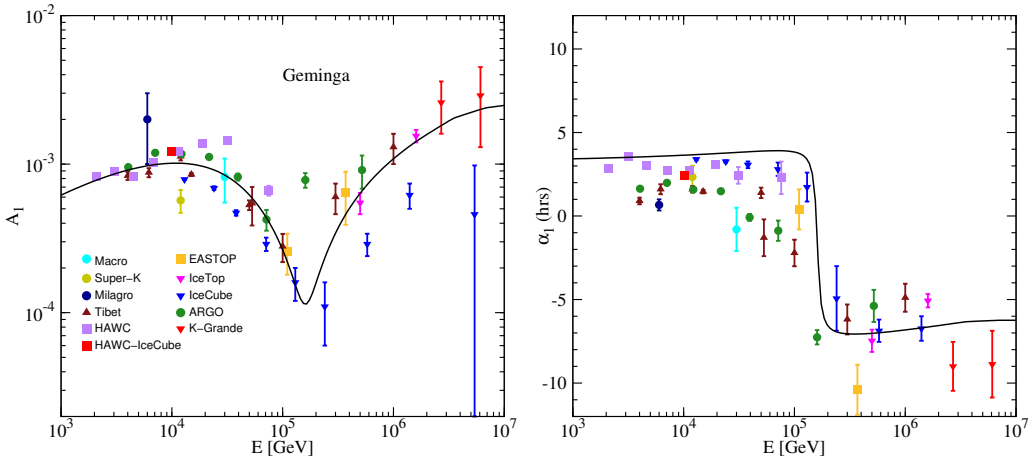

Figure 3. The energy dependences of the amplitude (**left**) and phase (**right**) of anisotropy with the contribution from Geminga SNR source. The data points are taken from Marco [75], Super-Kamiokande [24], EAS-TOP [34,76], Milagro [26], IceCube [27,29,31], Ice-Top [30], ARGO-YBJ [33], Tibet [22,23,77], KASCADE-Grande [35,36] HAWC [41], and HAWC-IceCube [41].

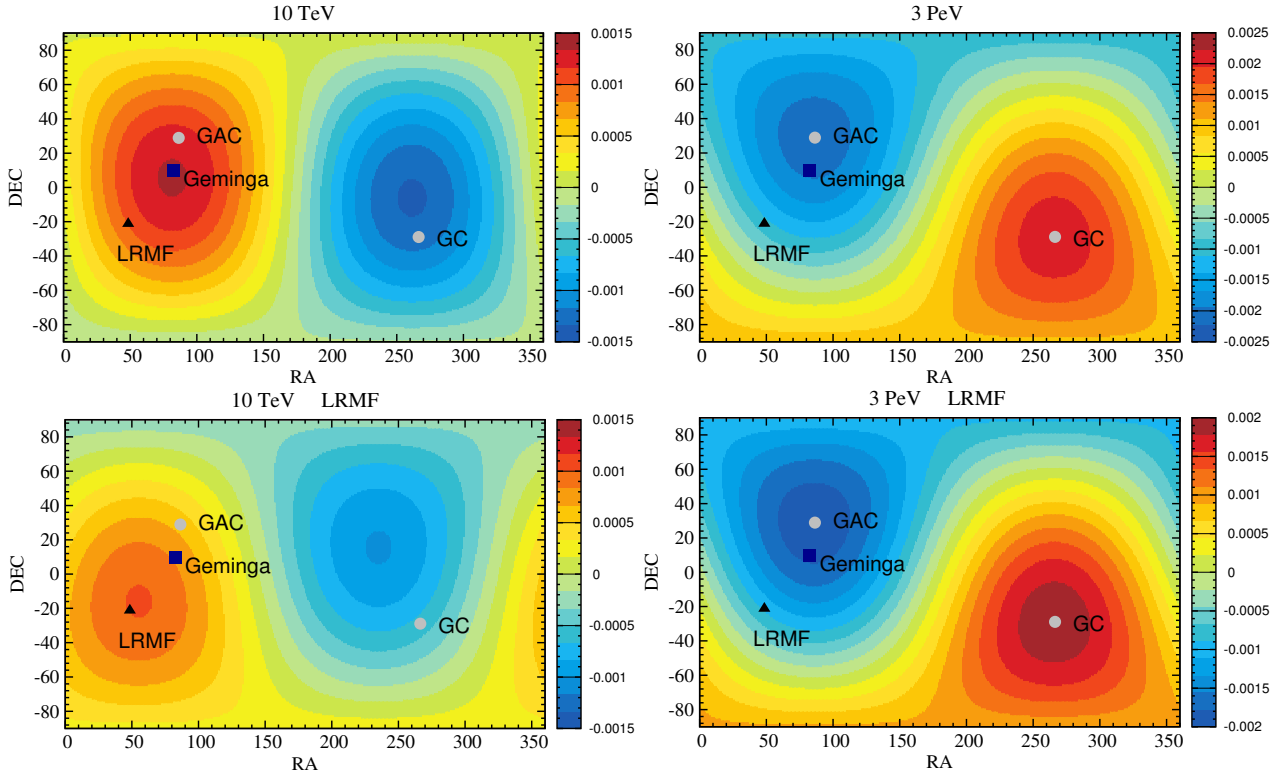

Figure 4. Two-dimensional anisotropy maps with the contribution from Geminga SNR source at 10 TeV (**left**) and 3 PeV (**right**), respectively. Top maps are 2D anisotropy under isotropic diffusion, and bottom maps are 2D anisotropy under anisotropic diffusion introduced by LRMF.

The solid black line in Figure 5 (left) shows the amplitude of anisotropy with the contribution from the Monogem SNR source. We found that the amplitude is greater than the experimental value. It is known that the spin-down energy of the Monogem pulsar is much lower than that of the Geminga pulsar with the value of $1.8 \times 10^{48}/1.25 \times 10^{49}$ erg, which suggests the injection power of the Monogem SNR is about one-tenth that of the Geminga SNR. Additionally, the gamma emission of the Monogem SNR is lower than that of the Geminga SNR, which also indicates that the injection power of the Monogem SNR is lower [60]. Therefore, we correct the injection power of Monogem according to

the spin-down energy of pulsars. The dashed black line in Figure 5 (left) indicates the corrected amplitude of anisotropy, which is lower than the experimental observation. We calculated the corrected proton spectrum again, as shown by the dashed line in Figure 5 (right). The corrected proton spectrum cannot explain the spectrum hardening at 200 GeV. Therefore, after considering the correction, the contribution of the Monogem SNR to energy spectra and anisotropy can be ignored.

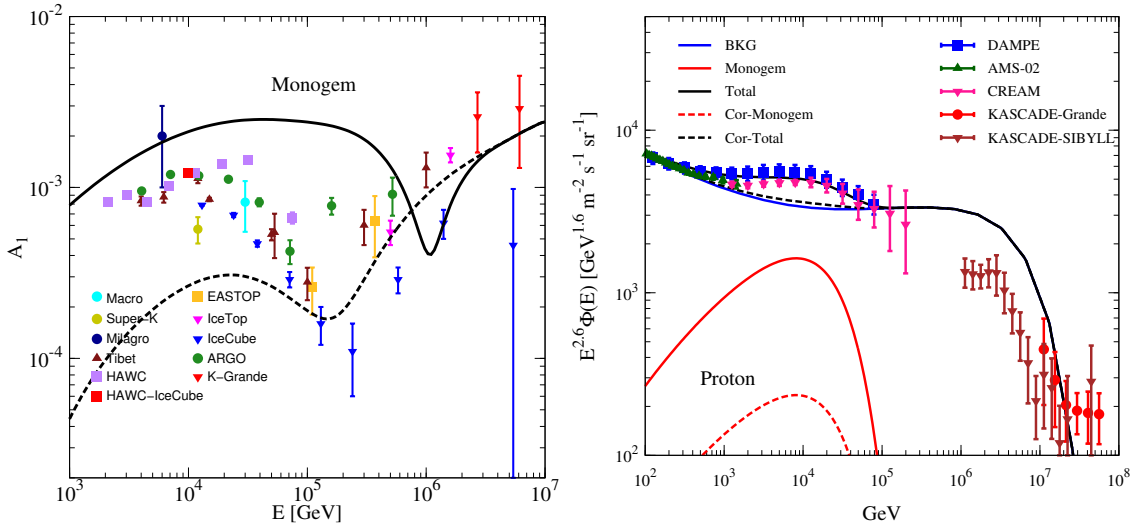

Figure 5. The amplitude of anisotropy (**left**) and proton spectra (**right**) with the contribution from Monogem SNR source, respectively. For the anisotropy, the black solid line is the result of model calculation, and the black dashed line displays the corrected anisotropy in accordance with the spin-down energy of the Geminga and the Monogem pulsars. For the energy spectra, the blue line represents the fluxes from the background sources, the red solid line represents the fluxes from the Monogem SNR, and the black solid line displays the sum contributions of the background and nearby sources. The dashed lines in the corresponding colors represent the corrected results.

Figure 6 shows the anisotropy with the contribution from the Loop I SNR source. It is clear that neither the amplitude nor phase agree with the measurements of the experiment. The Loop I source, located in the direction of the GC, is in the same direction as the background sources. So, their amplitude of synthesis increases as the energy increases; meanwhile, the phase always points toward the GC.

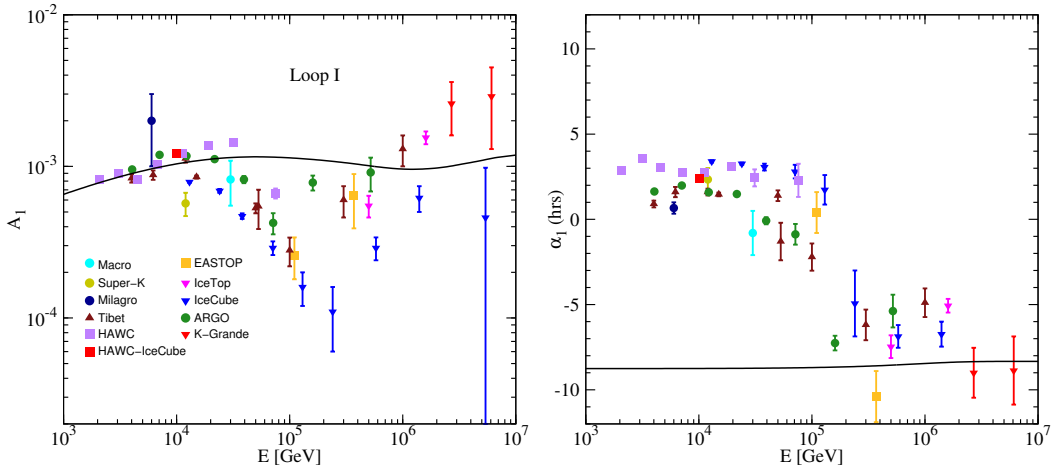

Figure 6. The amplitude (**left**) and phase (**right**) of anisotropy with the contribution from Loop I SNR source.

4. Summary

In recent years, a large number of detectors have detected the anomalous structures of CR spectra at 200 GeV and the complex energy dependence of anisotropy from 100 GeV to hundreds of PeV, which have been revealed to be related to nearby sources. The aim of this work is to explore the optimal nearby source using energy spectra and anisotropy as probes. Five nearby sources including Geminga, Monogem, Loop I, Vela, and Cygnus are used as research objects, and the SDP model, which introduces anisotropic diffusion caused by LRMF, is used in the calculation process. Since our previous work only calculated 1D anisotropy along the right ascension and the anisotropy of the declination direction was unknown, this work further provides 2D anisotropy maps along the right ascension and declination.

The CR spectra results indicate that only the older nearby sources such as Geminga, Monogem, and Loop I can explain the nuclear spectral hardening at ∼200 GeV, assuming a common injection power. Meanwhile, younger ones such as Vela and Cygnus cannot explain this phenomenon, mainly because the lower-energy CRs produced by them reach the solar system with difficulty.

The 2D anisotropy maps reveal that the LRMF significantly deflects CR particles below 100 TeV, while it has no effect on particles above the 100 TeV energy region. The combined influence of the nearby source and LRMF dominates the phase of anisotropy below 100 TeV. The Geminga SNR source is located at the anti-GC, below the galactic disk and near the LRMF direction, and its contributions to the energy spectrum and anisotropy agree well with the experimental observations. The anisotropy from the Monogem SNR is obviously higher than the observations. After correcting the injection power of the Monogem SNR in accordance with the spin-down energy of the Geminga and the Monogem pulsars, the contribution from the Monogem SNR can be ignored. The anisotropy of the Loop I source is clearly inconsistent with the experiment, because it is located in the direction of the GC. Therefore, the Geminga SNR source, which can simultaneously explain the proton and helium spectral hardening at ∼200 GeV and the anisotropy from 100 GeV to PeV energy region well, is the optimal nearby source, while the other sources cannot.

Author Contributions: Conceptualization, A.L. and Y.G.; methodology, A.L. and Y.G.; software, W.L.; validation, A.L. and W.L.; formal analysis, W.L.; investigation, Y.G.; resources, A.L.; data curation, A.L.; writing—original draft preparation, A.L. and Y.G.; writing—review and editing, A.L., W.L.; visualization, A.L.; supervision, Y.G. and W.L.; project administration, W.L.; funding acquisition, A.L. All authors have read and agreed to the published version of the manuscript.

Funding: This work is supported by the National Natural Science Foundation of China (U2031110, 12275279, 11963004) and the Shandong Province Natural Science Foundation (ZR2020MA095).

Data Availability Statement: Data are contained within the article.

Conflicts of Interest: The authors declare no conflicts of interest.

References

1. Ackermann, M.; Ajello, M.; Allafort, A.; Baldini, L.; Ballet, J.; Barbiellini, G.; Baring, M.G.; Bastieri, D.; Bechtol, K.; Bellazzini, R.; et al. Detection of the Characteristic Pion-Decay Signature in Supernova Remnants. *Science* **2013**, *339*, 807–811. [CrossRef]
2. Blasi, P. The origin of galactic cosmic rays. *A&A Rev.* **2013**, *21*, 70.
3. Panov, A.D.; Adams, J.H.; Ahn, H.S.; Batkov, K.E.; Bashindzhagyan, G.L.; Watts, J.W.; Panov, A.D.; Adams, J.H.; Ahn, H.S.; Batkov, K.E.; et al. Elemental energy spectra of cosmic rays from the data of the ATIC-2 experiment. *Bull. Russ. Acad. Sci. Phys.* **2007**, *71*, 494–497. [CrossRef]
4. Ahn, H.S.; Allison, P.; Bagliesi, M.G.; Beatty, J.J.; Bigongiari, G.; Childers, J.T.; Conklin, N.B.; Coutu, S.; DuVernois, M.A.; Ganel, O.; et al. Discrepant Hardening Observed in Cosmic-ray Elemental Spectra. *Astrophys. J. Lett* **2010**, *714*, L89–L93. [CrossRef]
5. Yoon, Y.S.; Ahn, H.S.; Allison, P.S.; Bagliesi, M.G.; Beatty, J.J.; Bigongiari, G.; Boyle, P.J.; Childers, J.T.; Conklin1, N.B.; Coutu, S.; et al. Cosmic-ray Proton and Helium Spectra from the First CREAM Flight. *Astrophys. J.* **2011**, *728*, 122. [CrossRef]
6. Adriani, O.; Barbarino, G.C.; Bazilevskaya, G.A.; Bellotti, R.; Boezio, M.; Bogomolov, E.A.; Bonechi, L.; Bongi, M.; Bonvicini, V.; Borisov, S.; et al. PAMELA Measurements of Cosmic-Ray Proton and Helium Spectra. *Science* **2011**, *332*, 69. [CrossRef]

7. Aguilar, M.; Aisa, D.; Alpat, B.; Alvino, A.; Ambrosi, G.; Andeen, K.; Arruda, L.; Attig, N.; Azzarello, P.; Bachlechner, A.; et al. Precision Measurement of the Proton Flux in Primary Cosmic Rays from Rigidity 1 GV to 1.8 TV with the Alpha Magnetic Spectrometer on the International Space Station. *Phys. Rev. Lett.* **2015**, *114*, 171103. [CrossRef] [PubMed]
8. Aguilar, M.; Aisa, D.; Alpat, B.; Alvino, A.; Ambrosi, G.; Andeen, K.; Arruda, L.; Attig, N.; Azzarello, P.; Bachlechner, A.; et al. Precision Measurement of the Helium Flux in Primary Cosmic Rays of Rigidities 1.9 GV to 3 TV with the Alpha Magnetic Spectrometer on the International Space Station. *Phys. Rev. Lett.* **2015**, *115*, 211101. [CrossRef] [PubMed]
9. Adriani, O.; Akaike, Y.; Asano, K.; Asaoka, Y.; Bagliesi, M.G.; Berti, E.; Bigongiari, G.; Binns, W.R.; Bonechi, S.; Bongi, M.; et al. Direct Measurement of the Cosmic-Ray Proton Spectrum from 50 GeV to 10 TeV with the Calorimetric Electron Telescope on the International Space Station. *Phys. Rev. Lett.* **2019**, *112*, 181102. [CrossRef] [PubMed]
10. DAMPE Collaboration; An, Q.; Asfandiyarov, R.; Azzarello, P.; Bernardini, P.; Bi, X.J.; Cai, M.S.; Chang, J.; Chen, D.Y.; Chen, H.F.; et al. Measurement of the cosmic ray proton spectrum from 40 GeV to 100 TeV with the DAMPE satellite. *Science* **2019** *5*, eaax3793.
11. Alemanno, F.; An, Q.; Azzarello, P.; Barbato, F.C.T.; Bernardini, P.; Bi, X.J.; Cai, M.S.; Catanzani, E.; Chang, J.; Chen, D.Y.; et al. Measurement of the Cosmic Ray Helium Energy Spectrum from 70 GeV to 80 TeV with the DAMPE Space Mission. *Phys. Rev. Lett.* **2021**, *126*, 201102. [CrossRef]
12. Yoon, Y.S.; Anderson, T.; Barrau, A.; Conklin, N.B.; Coutu, S.; Derome, L.; Han, J.H.; Jeon, J.A.; Kim, K.C.; Kim, M.H.; et al. Proton and Helium Spectra from the CREAM-III Flight. *Astrophys. J.* **2017**, *839*, 5. [CrossRef]
13. Atkin, E.; Bulatov, V.; Dorokhov, V.; Gorbunov, N.; Filippov, S.; Grebenyuk, V.; Karmanov, D.; Kovalev, I.; Kudryashov, I.; Kurganov, A.; et al. New Universal Cosmic-Ray Knee near a Magnetic Rigidity of 10 TV with the NUCLEON Space Observatory. *J. Exp. Theor. Phys. Lett.* **2018**, *108*, 5–12. [CrossRef]
14. Thoudam, S.; Hörandel, J.R. Nearby supernova remnants and the cosmic ray spectral hardening at high energies. *MNRAS* **2012**, *421*, 1209–1214. [CrossRef]
15. Liu, W.; Guo, Y.Q.; Yuan, Q. Indication of nearby source signatures of cosmic rays from energy spectra and anisotropies. *J. Cosmol. Astropart. Phys.* **2019**, *2019*, 010. [CrossRef]
16. Biermann, P.L.; Becker, J.K.; Dreyer, J.; Meli, A.; Seo, E.S.; Stanev, T. The Origin of Cosmic Rays: Explosions of Massive Stars with Magnetic Winds and Their Supernova Mechanism. *Astrophys. J.* **2010**, *725*, 184–187. [CrossRef]
17. Thoudam, S.; Rachen, J.P.; Van Vliet, A.; Achterberg, A.; Buitink, S.; Falcke, H.; Hörandel, J.R. Cosmic-ray energy spectrum and composition up to the ankle: The case for a second Galactic component. *Astron. Astrophys.* **2016**, *595*, A33. [CrossRef]
18. Tomassetti, N. Origin of the Cosmic-Ray Spectral Hardening. *Astrophys. J. Lett.* **2012**, *752*, L13. [CrossRef]
19. Yuan, Q.; Zhang, B.; Bi, X.J. Cosmic ray spectral hardening due to dispersion in the source injection spectra. *Phys. Rev. D.* **2011**, *84*, 043002. [CrossRef]
20. Zatsepin, V.I.; Sokolskaya, N.V. Three component model of cosmic ray spectra from 10 GeV to 100 PeV. *Astron. Astrophys.* **2006**, *458*, 1–5. [CrossRef]
21. Amenomori, M.; Ayabe, S.; Bi, X.J.; Chen, D.; Cui, S.W.; Danzengluobu; Ding, L.K.; Ding, X.H.; Feng, C.F.; Feng, Z.; et al. Anisotropy and Corotation of Galactic Cosmic Rays. *Science* **2006**, *314*, 439–443. [CrossRef]
22. Amenomori, M.; Bi, X.J.; Chen, D.; Cui, S.W.; Ding, L.K.; Ding, X.H.; Fan, C.; Feng, C.F.; Feng, Z.; Feng, Z.Y.; et al. On Temporal Variations of the Multi-TeV Cosmic Ray Anisotropy using the Tibet III Air Shower Array. *Astrophys. J.* **2010**, *711*, 119–124.
23. Amenomori, M.; Bi, X.J.; Chen, D.; Chen, T.L.; Chen, W.Y.; Cui, S.W.; Danzengluobu; Ding, L.K.; Feng, C.F.; Feng, Z.; et al. Northern Sky Galactic Cosmic Ray Anisotropy between 10 and 1000 TeV with the Tibet Air Shower Array. *Astrophys. J.* **2017**, *836*, 153. [CrossRef]
24. Guillian, G.; Hosaka, J.; Ishihara, K.; Kameda, J.; Koshio, Y.; Minamino, A.; Mitsuda, C.; Miura, M.; Moriyama, S.; Nakahata, M.; et al. Observation of the anisotropy of 10TeV primary cosmic ray nuclei flux with the Super-Kamiokande-I detector. *Phys. Rev. D* **2007**, *75*, 062003. [CrossRef]
25. Abdo, A.A.; Allen, B.; Aune, T.; Berley, D.; Blaufuss, E.; Casanova, S.; Chen, C.; Dingus, B.L.; Ellsworth, R.W.; Fleysher, L.; et al. Discovery of Localized Regions of Excess 10-TeV Cosmic Rays. *Phys. Rev. Lett.* **2008**, *101*, 221101. [CrossRef] [PubMed]
26. Abdo, A.A.; Allen, B.T.; Aune, T.; Berley, D.; Casanova, S.; Chen, C.; Dingus, L.; Ellsworth, R.W.; Fleysher, L.; Fleysher, R.; et al. The Large-Scale Cosmic-Ray Anisotropy as Observed with Milagro. *Astrophys. J.* **2009**, *698*, 2121–2130. [CrossRef]
27. Abbasi, R.; Abdou, Y.; Abu-Zayyad, T.; Adams, J.; Aguilar, J.A.; Ahlers, M.; Andeen, K.; Auffenberg, J.; Bai, X.; Baker, M.; et al. Measurement of the Anisotropy of Cosmic-ray Arrival Directions with IceCube. *Astrophys. J. Lett.* **2010**, *718*, L194–L198. [CrossRef]
28. Abbasi, R.; Abdou, Y.; Abu-Zayyad, T.; Adams, J.; Aguilar, J.A.; Ahlers, M.; Altmann, D.; Andeen, K.; Auffenberg, J.; Bai, X.; et al. Observation of Anisotropy in the Arrival Directions of Galactic Cosmic Rays at Multiple Angular Scales with IceCube. *Astrophys. J.* **2011**, *740*, 16. [CrossRef]
29. Abbasi, R.; Abdou, Y.; Abu-Zayyad, T.; Ackermann, M.; Adams, J.; Aguilar, J.A.; Ahlers, M.; Allen, M.M.; Altmann, D.; Andeen, K.; et al. Observation of Anisotropy in the Galactic Cosmic-Ray Arrival Directions at 400 TeV with IceCube. *Astrophys. J.* **2011**, *746*, 33. [CrossRef]
30. Aartsen, M.G.; Abbasi, R.; Abdou, Y.; Ackermann, M.; Adams, J.; Aguilar, J.A.; Ahlers, M.; Altmann, D.; Andeen, K.; Auffenberg, J.; et al. Observation of Cosmic-Ray Anisotropy with the IceTop Air Shower Array. *Astrophys. J.* **2013**, *765*, 55. [CrossRef]

31. Aartsen, M.G.; Abraham, K.; Ackermann, M.; Adams, J.; Aguilar, J.A.; Ahlers, M.; Ahrens, M.; Altmann, D.; Anderson, T.; Ansseau, I.; et al. Anisotropy in Cosmic-Ray Arrival Directions in the Southern Hemisphere Based on Six Years of Data from the IceCube Detector. *Astrophys. J.* **2016**, *826*, 220. [CrossRef]
32. Bartoli, B.; Bernardini, P.; Bi, X.J.; Bolognino, I.; Branchini, P.; Budano, A.; Calabrese Melcarne, A.K.; Camarri, P.; Cao, Z.; Cardarelli, R.; et al. Medium scale anisotropy in the TeV cosmic ray flux observed by ARGO-YBJ. *Phys. Rev. D* **2013**, *88*, 082001. [CrossRef]
33. Bartoli, B.; Bernardini, P.; Bi, X.J.; Cao, Z.; Catalanotti, S.; Chen, S.Z.; Chen, T.L.; Cui, S.W.; Dai, B.Z.; D'Amone, A.; et al. ARGO-YBJ Observation of the Large-scale Cosmic Ray Anisotropy During the Solar Minimum between Cycles 23 and 24. *Astrophys. J.* **2015**, *809*, 90. [CrossRef]
34. Aglietta, M.; Alekseenko, V.V.; Alessandro, B.; Antonioli, P.; Arneodo, F.; Bergamasco, L.; Bertaina, M.; Bonino, R.; Castellina, A.; Chiavassa, A.; et al. Evolution of the Cosmic-Ray Anisotropy Above 10^{14} eV. *Astrophys. J.* **2009**, *692*, L130–L133. [CrossRef]
35. Chiavassa, A.; Apel, W.; Arteaga-Velazquez, J.; Bekk, K.; Bertaina, M.; Blümer, J.; Bozdog, H.; Brancus, I.M.; Cantoni, E.; Cossavella, F.; et al. A study of the first harmonic of the large scale anisotropies with the KASCADE-Grande experiment. In Proceedings of the 34th International Cosmic Ray Conference (ICRC2015), Den Haag, The Netherlands, 30 July–6 August 2015; Volume 34, p. 281.
36. Apel, W.D.; Arteaga-Velázquez, J.C.; Bekk, K.; Bertaina, M.; Blümer, J.; Bonino, R.; Bozdog, H.; Brancus, I.M.; Cantoni1, E.; Chiavassa, A.; et al. Search for Large-scale Anisotropy in the Arrival Direction of Cosmic Rays with KASCADE-Grande. *Astrophys. J.* **2019**, *870*, 91. [CrossRef]
37. Abeysekara, A.U.; Alfaro, R.; Alvarez, C.; Álvarez, J.D.; Arceo, R.; Arteaga-Velázquez, J.C.; Solares, H.A.A.; Barber, A.S.; Baughman, B.M.; Bautista-Elivar, N.; et al. Observation of Small-scale Anisotropy in the Arrival Direction Distribution of TeV Cosmic Rays with HAWC. *Astrophys. J.* **2014**, *796*, 108. [CrossRef]
38. Abeysekara, A.U.; Alfaro, R.; Alvarez, C.; Álvarez, J.D.; Arceo, R.; Arteaga-Velázquez, J.C.; Rojas, D.A.; Solares, H.A.A.; Becerril, A.; Belmont-Moreno, E.; et al. Observation of Anisotropy of TeV Cosmic Rays with Two Years of HAWC. *Astrophys. J.* **2018**, *865*, 57. [CrossRef]
39. Funsten, H.O.; DeMajistre, R.; Frisch, P.C.; Heerikhuisen, J.; Higdon, D.M.; Janzen, P.; Larsen, B.A.; Livadiotis, G.; McComas, D.J.; Möbius, E.; et al. Circularity of the Interstellar Boundary Explorer Ribbon of Enhanced Energetic Neutral Atom (ENA) Flux. *Astrophys. J.* **2013**, *776*, 30. [CrossRef]
40. Li, A.; Yin, S.; Liu, M.; Wang, H.; Li, X.; Li, Y. Interpretation of the Spectra and Anisotropy of Galactic Cosmic Rays. *Universe* **2022**, *8*, 307. [CrossRef]
41. Abeysekara, A.U.; Alfaro, R.; Alvarez, C.; Arceo, R.; Arteaga-Velázquez, J.C.; Rojas, D.A.; Belmont-Moreno, E.; BenZvi, S.Y.; Brisbois, C.; Capistrán, T.; et al. All-sky Measurement of the Anisotropy of Cosmic Rays at 10 TeV and Mapping of the Local Interstellar Magnetic Field. *Astrophys. J.* **2019**, *871*, 96. [CrossRef]
42. Ahlers, M. Deciphering the Dipole Anisotropy of Galactic Cosmic Rays. *Phys. Rev.* **2016**, *117*, 151103. [CrossRef] [PubMed]
43. Compton, A.H.; Getting, I.A. An Apparent Effect of Galactic Rotation on the Intensity of Cosmic Rays. *Phys. Rev.* **1935**, *47*, 817–821. [CrossRef]
44. Luo, Q.; Qiao, B.Q.; Liu, W.; Cui, S.W.; Guo, Y.Q. Statistical Study of the Optimal Local Sources for Cosmic Ray Nuclei and Electrons. *Astrophys. J.* **2022**, *930*, 82. [CrossRef]
45. Zhao, B.; Liu, W.; Yuan, Q.; Hu, H.B.; Bi, X.J.; Wu, H.R.; Zhou, X.-X.; Guo, Y.-Q. Geminga SNR: Possible Candidate of the Local Cosmic-Ray Factory. *Astrophys. J.* **2022**, *926*, 41. [CrossRef]
46. Tang, T.P.; Xia, Z.Q.; Shen, Z.Q.; Zu, L.; Feng, L.; Yuan, Q.; Fan, Y.-Z.; Wu, J. Explanation of nearby SNRs for primary electron excess and proton spectral bump. *Phys. Lett. B.* **2022**, *825*, 13684. [CrossRef]
47. Schwadron, N.A.; Adams, F.C.; Christian, E.R.; Desiati, P.; Frisch, P.; Funsten, H.O.; Jokipii, J.R.; McComas, D.J.; Moebius, E.; Zank, G.P. et al. Global Anisotropies in TeV Cosmic Rays Related to the Sun's Local Galactic Environment from IBEX. *Science* **2014**, *343*, 988–990. [CrossRef]
48. Liu, W.; Lin, S.J.; Hu, H.; Guo, Y.Q.; Li, A.F. Two Numerical Methods for the 3D Anisotropic Propagation of Galactic Cosmic Rays. *ApJ* **2020**, *892*, 6. [CrossRef]
49. Caraveo, P.A.; Bignami, G.F.; Mignani, R; Taff, L.G. Parallax Observations with the Hubble Space Telescope Yield the Distance to Geminga *Astrophys. J. Lett.* **1996**, *461*, L91. [CrossRef]
50. Plucinsky, P.P.; Snowden, S.L.; Aschenbach, B.; Egger, R.; Edgar, R.J.; McCammon, D. ROSAT Survey Observations of the Monogem Ring. *Astrophys. J.* **1996**, *463*, 224. [CrossRef]
51. Cha, A.N.; Sembach, K.R.; Danks, A.C. The Distance to the Vela Supernova Remnant. *Astrophys. J.* **1999**, *515*, L25–L28. [CrossRef]
52. Egger, R.J.; Aschenbach, B. Interaction of the Loop I supershell with the Local Hot. *Astron. Astrophys.* **1995**, *294*, L25–L28.
53. Sun, X.H.; Reich, W.; Han, J.L.; Reich, P.; Wielebinski, R. New λ6 cm observations of the Cygnus Loop. *Astron. Astrophys.* **2006**, *447*, 937–947 [CrossRef]
54. Andrew, W.S.; Igor, V.M.; Vladimir, S.P. Cosmic-Ray Propagation and Interactions in the Galaxy. *Annu. Rev. Nucl. Part. Sci.* **2007**, *27*, 285–327.
55. Tomassetti, N. Cosmic-ray protons, nuclei, electrons, and antiparticles under a two-halo scenario of diffusive propagation. *Phys. Rev. D* **2015**, *92*, 8. [CrossRef]
56. Feng, J. Tomassetti Nicola and Oliva Alberto. Bayesian analysis of spatial-dependent cosmic-ray propagation: Astrophysical background of antiprotons and positrons. *Phys. Rev. D* **2016**, *94*, 12. [CrossRef]

57. Guo, Y.-Q.; Tian, Z.; Jin, C. Spatial-dependent Propagation of Cosmic Rays Results in the Spectrum of Proton, Ratios of P/P, and B/C, and Anisotropy of Nuclei. *Astrophys. J.* **2016**, *819*, 54. [CrossRef]
58. Liu, W.; Yao, Y.-h.; Guo, Y.-Q. Revisiting the Spatially Dependent Propagation Model with the Latest Observations of Cosmic-Ray Nuclei. *Astrophys. J.* **2018**, *869*, 176. [CrossRef]
59. Guo, Y.-Q.; Yuan, Q. Understanding the spectral hardenings and radial distribution of Galactic cosmic rays and Fermi diffuse γ rays with spatially-dependent propagation. *Phys. Rev. D* **2018**, *97*, 063008. [CrossRef]
60. Abeysekara, A.U.; Albert, A.; Alfaro, R.; Alvarez, C.; Álvarez, J.D.; Arceo, R.; Arteaga-Velázquez, J.C.; Rojas, D.A.; Solares, H.A.A.; Barber, A.S.; et al. Extended gamma-ray sources around pulsars constrain the origin of the positron flux at Earth. *Science* **2017**, *358*, 6365. [CrossRef]
61. Aharonian, F.; An, Q.; Bai, L.X.; Bai, Y.X.; Bao, Y.W.; Bastieri, D.; Bastieri, D.; Bi, X.J.; Bi, Y.J.; Cai, H.; et al. Extended Very-High-Energy Gamma-Ray Emission Surrounding PSR J 0622 +3749 Observed by LHAASO-KM2A. *Phys. Rev. Lett.* **2021**, *126*, 24. [CrossRef]
62. Evoli, C.; Gaggero, D.; Grasso, D.; Maccione, L. Cosmic Ray propagation in the Galaxy and diffuse gamma-ray emission. *Am. Inst. Phys. Conf. Series.* **2008**, *1085*, 380–383.
63. Case, G.; Bhattacharya, D. Revisiting the galactic supernova remnant distribution. *Astron. Astrophys. Suppl.* **1996**, *120*, 437–440.
64. Blasi, P.; Amato, E. Diffusive propagation of cosmic rays from supernova remnants in the Galaxy. II: Anisotropy. *J. Cosmol. Astropart. Phys.* **2012**, *1*, 11. [CrossRef]
65. Sveshnikova, L.G.; Strelnikova, O.N.; Ptuskin, V.S. Spectrum and anisotropy of cosmic rays at TeV-PeV-energies and contribution of nearby sources. *Astropart. Phys.* **2013**, *50*, 33–46. [CrossRef]
66. Giacalone, J.; Jokipii, J.R. The Transport of Cosmic Rays across a Turbulent Magnetic Field. *ApJ* **1999**, *520*, 204–214. [CrossRef]
67. Cerri, S.S.; Gaggero, D.; Vittino, A.; Evoli, C.; Grasso, D. A signature of anisotropic cosmic-ray transport in the gamma-ray sky. *J. Cosmol. Astropart. Phys.* **2017**, *10*, 019. [CrossRef]
68. Snodin, A.P.; Shukurov, A.; Sarson, G.R.; Bushby, P.J.; Rodrigues, L.F.S. Global diffusion of cosmic rays in random magnetic fields. *Mon. Not. R. Astron. Soc.* **2016**, *457*, 3975–3987. [CrossRef]
69. De Marco, D.; Blasi, P.; Stanev, T. Numerical propagation of high energy cosmic rays in the Galaxy: I. Technical issues. *J. Cosmol. Astropart. Phys.* **2007**, *6*, 027. [CrossRef]
70. Aguilar, M.; Cavasonza, L.A.; Ambrosi, G.; Arruda, L.; Attig, N.; Aupetit, S.; Azzarello, P.; Bachlechner, A.; Barao, F.; Barrau, A.; et al. Precision Measurement of the Boron to Carbon Flux Ratio in Cosmic Rays from 1.9 GV to 2.6 TV with the Alpha Magnetic Spectrometer on the International Space Station. *Phys. Rev. Lett.* **2016**, *117*, 231102. [CrossRef]
71. Aguilar, M.; Cavasonza, L.A.; Alpat, B.; Ambrosi, G.; Arruda, L.; Attig, N.; Aupetit, S.; Azzarello, P.; Bachlechner, A.; Barao, F.; et al. Observation of the Identical Rigidity Dependence of He, C, and O Cosmic Rays at High Rigidities by the Alpha Magnetic Spectrometer on the International Space Station. *Phys. Rev. Lett.* **2017**, *119*, 251101. [CrossRef]
72. Atkin, E.; Bulatov, V.; Dorokhov, V.; Gorbunov, N.; Filippov, S.; Grebenyuk, V.; Karmanov, D.; Kovalev, I.; Kudryashov, I.; Kurganov, A.; et al. First results of the cosmic ray NUCLEON experiment. *J. Cosmol. Astropart. Phys.* **2017**, *2017*, 020. [CrossRef]
73. Antoni, T.; Apel, W.D.; Badea, A.F.; Bekk, K.; Bercuci, A.; Blümer, J.; Bozdog, H.; Brancus, I.M.; Chilingarian, A.; Daumiller, K.; et al. KASCADE measurements of energy spectra for elemental groups of cosmic rays: Results and open problems. *Astropart. Physics.* **2005**, *24*, 1–25. [CrossRef]
74. Apel, W.D.; Arteaga-Velázquez, J.C.; Bekk, K.; Bertaina, M.; Blümer, J.; Bozdog, H.; Brancus, I.M.; Cantoni, E.; Chiavassa, A.; Cossavella, F.; et al. KASCADE-Grande measurements of energy spectra for elemental groups of cosmic rays. *Astropart. Phys.* **2013**, *47*, 54–66. [CrossRef]
75. Ambrosio, M.; Antolini, R.; Baldini, A.; Barbarino, G.C.; Barish, B.C.; Battistoni, G.;Becherini, Y.; Bellotti, R.; Bemporad, C.; Bernardini, P.; et al. Search for the sidereal and solar diurnal modulations in the total MACRO muon data set. *Phys. Rev. D* **2003**, *67*, 042002. [CrossRef]
76. Aglietta, M.; Alessandro, B.; Antonioli, P.; Arneodo, F.; Bergamasco, L.; Bertaina, M. Study of the Cosmic Ray Anisotropy at Eo ∼100 TeV from EAS-TOP: 1992–1994. *Int. Cosmic Ray Conf.* **1995**, *2*, 800.
77. Amenomori, M.; Ayabe, S.; Cui, S.W.; Danzengluobu; Ding, L.K.; Ding, X.H.; Feng, C.F.; Feng, Z.Y.; Gao, X.Y.; Geng, X.Q.; et al. Large-Scale Sidereal Anisotropy of Galactic Cosmic-Ray Intensity Observed by the Tibet Air Shower Array. *Astrophys. J.* **2005**, *626*, L29–L32. [CrossRef]